HHS Public Access

Author manuscript

Biomed Phys Eng Express. Author manuscript; available in PMC 2022 March 28.

Published in final edited form as:

Biomed Phys Eng Express. ; 6(6): . doi:10.1088/2057-1976/abb834.

Sparse-view, short-scan, dedicated cone-beam breast computed tomography: Image quality assessment

Hsin Wu Tseng[1], **Andrew Karellas**[1], **Srinivasan Vedantham**[1,2,*]

[1]Department of Medical Imaging, The University of Arizona, Tucson, AZ

[2]Department of Biomedical Engineering, The University of Arizona, Tucson, AZ

Abstract

The purpose of this study is to quantify the impact of sparse-view acquisition in short-scan trajectories, compared to 360-degrees full-scan acquisition, on image quality measures in dedicated cone-beam breast computed tomography (BCT). Projection data from 30 full-scan (360-degrees; 300 views) BCT exams with calcified lesions were selected from an existing clinical research database. Feldkamp-Davis-Kress (FDK) reconstruction of the full-scan data served as the reference. Projection data corresponding to two short-scan trajectories, 204 and 270-degrees, which correspond to the minimum and maximum angular range achievable in a cone-beam BCT system were selected. Projection data were retrospectively sampled to provide 225, 180, and 168 views for 270-degrees short-scan, and 170 views for 204-degrees short-scan. Short-scans with 180 and 168 views in 270-degrees used non-uniform angular sampling. A fast, iterative, total variation-regularized, statistical reconstruction technique (FIRST) was used for short-scan image reconstruction. Image quality was quantified by variance, signal-difference to noise ratio (SDNR) between adipose and fibroglandular tissues, full-width at half-maximum (FWHM) of calcifications in two orthogonal directions, as well as, bias and root-mean-squared-error (RMSE) computed with respect to the reference full-scan FDK reconstruction. The median values of bias (8.6×10^{-4} – 10.3×10^{-4} cm^{-1}) and RMSE (6.8×10^{-6} – 9.8×10^{-6} cm^{-1}) in the short-scan reconstructions, computed with the full-scan FDK as the reference were close to, but not zero ($P<0.0001$, one-sample median test). The FWHM of the calcifications in the short-scan reconstructions did not differ significantly from the reference FDK reconstruction ($P>0.118$), except along the superior-inferior direction for the short-scan reconstruction with 168 views in 270-degrees ($P=0.046$). The variance and SDNR from short-scan reconstructions were significantly improved compared to the full-scan FDK reconstruction ($P<0.0001$). This study demonstrates the feasibility of the short-scan, sparse-view, compressed sensing-based iterative reconstruction. This study indicates that shorter scan times and reduced radiation dose without sacrificing image quality are potentially feasible.

*Contact information: Srinivasan Vedantham, PhD, DABR, FAAPM, Professor, Medical Imaging (DMI) and Biomedical Engineering (BME), The University of Arizona, 1501 N Campbell Ave, PO Box 245067, Tucson, AZ 85724-5067. Telephone: (520) 626-6641, Fax: (520) 626-2643, svedantham@radiology.arizona.edu.

Keywords

Breast cancer; dedicated breast CT; short-scan; sparse-view; statistical image reconstruction; image quality

1. INTRODUCTION

Cone-beam computed tomography (CBCT) enables three-dimensional (3D) and relatively low-dose, high-spatial resolution visualization for many applications including interventional, head, neck and extremity imaging. Dedicated cone-beam breast CT (BCT), a relatively new and highly specialized application of CBCT, generates tomographic and fully 3D images in any plane. Unlike digital mammography (Pisano *et al.*, 2005; Vedantham *et al.*, 2000a; Suryanarayanan *et al.*, 2002; Vedantham *et al.*, 2000b) and digital breast tomosynthesis (Niklason *et al.*, 1997; Suryanarayanan *et al.*, 2000; Michaelsen *et al.*, 2015; Vedantham *et al.*, 2015a; Friedewald *et al.*, 2014), BCT does not require breast compression. The masking of a suspicious area due to overlapping tissues is minimized in BCT (Chen *et al.*, 2013; Chen *et al.*, 2015; Vedantham *et al.*, 2012b; Vedantham *et al.*, 2013b). BCT also overcomes the various artifacts observed in DBT (Sujlana *et al.*, 2018). Current dedicated cone-beam BCT scanners use flat-panel detectors and acquire either 300 views (O'Connell *et al.*, 2010; O'Connell *et al.*, 2018; O'Connell *et al.*, 2014; Vedantham *et al.*, 2014) or 500 views (Lindfors *et al.*, 2008; Prionas *et al.*, 2010; Aminololama-Shakeri *et al.*, 2019) in a circular scan trajectory covering 360 degrees. The acquired projection data is reconstruction using the traditional Feldkamp-Davis-Kress (FDK) algorithm (Feldkamp *et al.*, 1984). One cone-beam BCT system, which acquires 300 views in 360-degrees (full-scan) has shown to improve sensitivity compared to mammography (Cole *et al.*, 2015) in a diagnostic setting and has obtained regulatory approvals in several countries and regions. The radiation dose to the breast in diagnostic setting from this cone-beam BCT system is approximately similar to diagnostic mammography, but is twice the limit from standard 2-view screening mammogram for a breast with an assumed average thickness and density (Vedantham *et al.*, 2013c). The radiation dose to the breast can be reduced in a number of ways; including optimization of the technique factors used for image acquisition (Hernandez *et al.*, 2020), by using beam shaping filters (Luck *et al.*, 2013; Vedantham *et al.*, 2015b; Vedantham and Karellas, 2017) and with novel image reconstruction techniques (Bian *et al.*, 2014; Tseng *et al.*, 2020).

In current cone-beam BCT designs, the x-ray tube travels in front of the patient head for 360 degree acquisition. This geometry uses a table-top design that requires the patient to turn the head sideways. Discomfort in the neck and shoulder was reported by a substantial proportion (9/23, 39%) of study participants with cone-beam BCT (O'Connell *et al.*, 2010). An appropriately designed short scan x-ray source trajectory that is inferior to the breast does not require the patient to turn their head, mitigating patient discomfort (Fig 1A). Developing a BCT system using the short-scan approach (270° or less) is very useful in dose reduction in dedicated BCT using either prone or upright patient positioning (Vedantham *et al.*, 2013a). Approximately 25% of women aged 65 years or more, and 15.4% of women aged 50 years or more, suffer from osteoporosis of the femoral neck or lumbar spine (Wright

et al., 2014), which makes prone positioning difficult. This allows for a more comfortable position for the patient and potentially for better positioning of the breast for maximizing inclusion of tissue near the chest-wall (Vedantham *et al.*, 2013a). Thus, the short-scan trajectory provides benefits for both prone and upright patient positioning (Vedantham *et al.*, 2013a). These factors served as our motivation for pursuing the short-scan trajectory in cone-beam BCT.

In short-scan, sparse-view CBCT, although the FDK algorithm provides fast reconstructions, it lacks of the ability to compensate for the missing projection data, and this generates streak artifacts and noisy images even with the use of Parker weights (Parker, 1982; Wesarg *et al.*, 2002), in particular for sparse-view acquisitions. Compressed sensing (CS) algorithms (Candes *et al.*, 2006; Candes and Tao, 2006) provide a more robust solution and they are effective in compensating for missing data in undersampling conditions. One of the important strategies of applying CS in image reconstruction is the total variation (TV) (Rudin *et al.*, 1992; Strong and Chan, 2003; Chambolle, 2004) approach based upon projection onto convex sets (POCS) (Sezan, 1992), which is able to effectively handle the insufficient or incomplete data sets. Among many extended algorithms based on the TV-POCS, the adaptive steepest descent-projection onto convex sets (ASD-POCS) algorithm (Sidky and Pan, 2008) has been proposed for CBCT and has been explored for cone-beam BCT (Bian *et al.*, 2014). In this study, we investigate a variant of this algorithm, referred to as Fast, Iterative, TV-Regularized, Statistical reconstruction Technique (FIRST), for image reconstruction (Tseng *et al.*, 2020). Although short-scan cone-beam acquisition have been used for other clinical applications (e.g., interventional imaging, positioning verification in radiation therapy, etc.) and applying this data acquisition for BCT may sound naïve; BCT must meet different imaging performance requirements compared to the aforementioned applications. For example, the clinical tasks associated with interventional imaging (often with administered contrast media) such as evaluation of percent stenosis or lesion size and guidance for endovascular device placement are substantially different from the clinical needs for breast imaging that are based on detecting and characterizing lesions. The ability to visualize microcalcifications and at a radiation dose suitable for breast cancer screening makes such acquisition and reconstruction challenging for BCT. To our knowledge, there are no publications that address image quality and potential dose reduction using the combination of short-scan and sparse-view approach on clinical cone-beam breast CT data.

In this study, we investigate the effect of incomplete projection datasets acquired by the short-scan and sparse-view approach on image quality in dedicated cone-beam BCT. The objectives are to determine (i) if it is feasible to reduce radiation dose with the combination of short-scan trajectory, sparse views, and iterative reconstruction while maintaining quantitative image quality similar to full-scan FDK reconstruction, and (ii) to determine the sparsity (number of views) that provide the best quantitative image quality for 270° and 204° short-scan trajectories, subject to the constraints of the available clinical datasets. The remaining part of this paper is organized as follows. In section 2, the method for generating for the short-scan and sparse-view projection data is described, followed by a brief discussion of the image reconstruction algorithm (FIRST). The image quality metrics used for evaluation are also addressed in this section. In the section 3, results from the quantitative image quality evaluation are reported.

2. METHODS AND MATERIALS

2.A. Clinical datasets

This retrospective study was conducted in accordance with an institutional review board (IRB)-approved protocol (Protocol # 1903470973) and used de-identified datasets from subjects who had participated in a prior clinical trial (ClinicalTrials.gov Identifier: NCT01090687). The cone-beam BCT datasets (Vedantham *et al.*, 2012a; Shi *et al.*, 2013) were acquired at 49 kV, 1.4 mm of Al 1st half-value layer thickness, 8 ms pulse-width, and 300 projection views over 360° (full-scan) with uniform angular sampling (1.2°) on a cone-beam BCT system (Pre-FDA approval prototype of KBCT1000, Koning Corp., West Henrietta, NY). This system used a RAD71-SP (Varian Medical Systems, Salt Lake City, UT) x-ray tube with a nominal focal spot size of 0.3 mm and a PaxScan 4030CB CsI:Tl scintillator coupled, amorphous silicon-based flat-panel detector (Varian Medical Systems, Salt Lake City, UT). The detector had a 1024×768 pixel matrix with native pixel size of 0.194 mm and was operated in a 2×2 binning mode to provide 0.388 mm pixels. The source-to-axis of rotation (AOR) distance (SAD) and the source-to-detector distance (SDD) were 650 mm and 898 mm, respectively. The standard image reconstruction provided by the system for clinical interpretation uses a 1024×1024 in-plane voxel matrix with 0.273 mm isotropic voxel sampling. For this study, a cohort of 30 cases with microcalcifications were selected. These 30 cases were a subset of the cases (53% with calcifications) used in the reader study with 18 radiologists that showed improved sensitivity of BCT (full-scan, FDK reconstruction) over mammography in diagnostic setting (Cole *et al.*, 2015). While the average glandular dose (AGD) from BCT was comparable to diagnostic (not screening) mammography, it was approximately twice that of standard 2-view mammography (Vedantham *et al.*, 2013c). Lindfors et al. reported that when the AGD to the breast from BCT is in the range of the standard 2-view mammography, then the conspicuity of calcified lesions is reduced in cone-beam BCT (Lindfors *et al.*, 2008), but did not investigate if this affected diagnostic performance measures such as sensitivity or specificity. Since, objective of the study is to investigate short-scan trajectories which lead to dose reduction, we focused on calcified lesions for this study. For the selected cohort of 30 cases with calcified lesions, the breast dimensions, the volumetric glandular fraction (Vedantham *et al.*, 2012a) and the AGD (Vedantham *et al.*, 2013c) from the full-scan acquisition are summarized in Table 1.

2.B. Short-scan and sparse-views

For short-scan BCT, several system geometric parameters (Fig 1B) need to be considered, including the distances from the source to axis-of-rotation (SAD), source to detector (SDD), and the swale-depth (S_d) of the protective cover. Also, the anode target angle of the x-ray tube and consequently the cone-beam extent of the x-ray beam needs to be factored. We utilized the body habitus and breast dimensions data (Vedantham *et al.*, 2013a), in conjunction with all technical parameters (tube output, anode angle) to design the system, which resulted in full fan-angle of 24°. Thus, an x-ray source trajectory encompassing an angular range of $2\alpha \geq 204°$ is needed to satisfy the data-sufficiency conditions for the central plane (Tuy, 1983). Also, factoring the acceleration and deceleration of the gantry and the space required to position the patient's head, the maximum angular range for the x-ray

source trajectory was determined to be 270°. In this study, we considered two representative cases of 2α = 204° and 2α = 270° corresponding to the minimum and maximum angular range for the, x-ray source trajectory. It is relevant to note that the short-scan, sparse-view acquisition can be implemented easily for both prone and upright patient positions.

For the two short-scan trajectories of 204° and 270°, uniform angular sampling interval of 1.2° matching the acquired clinical projection data were selected, resulting in 170 and 225 projection views, respectively. By experimenting with different starting angles, no differences were observed in the reconstructed images. Hence, for simplification, the projection view corresponding to 0° was selected as the starting angle for both 270° and 204° short-scan trajectories. Since the clinical projection data were acquired with 1.2°, we also considered 2.4° angular interval which maintains uniform angular sampling, but the image quality was poor and hence was excluded from the study. To consider different dose reduction levels, 80% and 75% of the 225 views were chosen for 270° short-scan, which resulted in 180 and 168 views, respectively. This was achieved by excluding the 3rd view within every 5 adjacent views for 180 views and the 3rd view within every 4 adjacent views for 168 views in the anticlockwise direction (Fig 2). This periodically missing projection views lead to datasets with non-uniform angular sampling. Although it has been reported that uniform/regular view-sampling method (for 360° full-scan) leads guarantee recovery (Jorgensen and Sidky, 2015) in full-scan (360°), this non-uniform angular sampling method was used for 180-views and 168-views in 270° short-scan due to the limitation of the available datasets. For the 204° short-scan, number of projection views less than 170 was not considered because of the substantial degradation in image quality. Thus, a total of four short-scan acquisition schemes were investigated.

2.C. Image reconstruction

The full-scan (300 views over 360°) projection datasets were reconstructed using FDK algorithm with ramp filter and served as the reference for image quality evaluation. The use of FDK reconstructions as the reference is appropriate, as this has shown higher sensitivity over digital mammography in diagnostic setting (Cole *et al.*, 2015).

The short-scan projection datasets can be approximately reconstructed using analytical methods such as the FDK reconstruction with Parker weights (Parker, 1982; Wesarg *et al.*, 2002). However, we observed substantial artifacts as seen in Fig 3. Hence, the short-scan projection datasets were reconstructed using the FIRST algorithm (Tseng *et al.*, 2020), which is a modified version of the ASD-POCS algorithm (Sidky and Pan, 2008). Interference-like artifacts can be observed in full field-of-view (28 cm × 28 cm) reconstructions (Tseng *et al.*, 2020) using ASD-POCS and can be mitigated by finer sampling of the voxel grid (Zbijewski and Beekman, 2004). However, there is concomitant increase in reconstruction time, which, even with graphics processing unit (GPU)-acceleration, made it impractical for the real-time interpretation needs for diagnostic breast imaging (Tseng *et al.*, 2020). Hence, in the FIRST algorithm, in addition to GPU acceleration, the combination of initializing with FDK reconstruction and using ordered subsets-simultaneous algebraic reconstruction technique (OS-SART) (Wang and Jiang, 2004; Gregor and Fessler, 2015) with 1 subset, instead of the algebraic reconstruction

technique (ART) (Gordon *et al.*, 1970) in the TV regularization step were implemented, and was shown to effectively suppress the artifacts without degrading the image quality and the spatial resolution (Tseng *et al.*, 2020). Substantial acceleration of the reconstruction process was also observed with the FIRST algorithm (Tseng *et al.*, 2020). Since convergence and reasonable image quality by visual inspection can be attained at early iterations (Bian *et al.*, 2010), unless stated otherwise 100 iterations were used consistently. For the projection and back projection step, representative methods for GPU-accelerated voxel-driven (Peters, 1981; Biguri, 2018), ray-driven (Biguri, 2018; Siddon, 1985), and distance-driven (Liu *et al.*, 2017) approaches were studied. The voxel and ray-driven methods are provided with the TIGRE-toolbox (Biguri *et al.*, 2016; Biguri, 2018) and we implemented the distance-driven method. All reconstructions were full field-of-view (28 cm × 28 cm) with 1024 × 1024 in-plane voxel matrix and with 0.273 mm isotropic voxel pitch. All reconstructions were performed on a single workstation employing a single GPU (Quadro P6000, NVidia Corporation, Santa Clara, CA) with 3840 cores and used the GPU-based TIGRE toolbox implementation (Biguri *et al.*, 2016) for the entire image reconstruction process.

2.D. Image quality metrics

Traditional image quality metrics such as noise, signal-difference to noise ratio (SDNR), the full-width at half-maximum (FWHM) of calcifications were computed for all reconstructions including the reference FDK reconstruction with full-scan projection data. Bias and root-mean squared error (RMSE) for the short-scan reconstructions were computed with the full-scan FDK reconstruction as the reference. All quantitative evaluations were performed on images in linear attenuation coefficients (units of 1/cm) and prior to transformation to Hounsfield Units (HU).

All cases in this study had microcalcifications. From the reference FDK reconstruction, the slice that best depicted the largest calcification in the cluster was identified for each case. The identified slice was used to quantify noise, SDNR and FWHM across all reconstructions. A fixed region-of-interest (ROI) size of 32×32 pixels was used to quantify the mean signal and noise in the adipose (black box in Fig. 4) and the fibroglandular (white box in Fig 4) regions. For each case, the ROI location was maintained consistently across all reconstructions. Noise was calculated by the variance (σ_A^2) in the adipose region. SDNR was computed as the ratio of the absolute difference in the mean signal between fibroglandular $(\overline{\mu_G})$ and adipose $(\overline{\mu_A})$ regions to the square-root of the average of the variances in these regions as expressed below:

$$SDNR = \frac{|\overline{\mu_G} - \overline{\mu_A}|}{\sqrt{\frac{1}{2}(\sigma_A^2 + \sigma_G^2)}} \quad (1)$$

Where, σ_G^2 is the variance in the fibroglandular region. The FWHM of the largest calcification (arrow in Fig 4) in each case was computed along the two orthogonal directions; the mediolateral direction, denoted as $FWHM_{ML}$ and the superior-inferior

direction, denoted as $FWHM_{SI}$. The largest calcification was chosen to improve the reliability of the FWHM estimate.

Bias was defined as the mean of the absolute difference in pixel values between the reference FDK and the FIRST images within the breast defined by the image mask (Fig 4b). This was computed as:

$$bias = \frac{1}{N}\sum_{i=1}^{N}\left|\mu_{ref,i} - \mu_{FIRST,i}\right| \quad (2)$$

Where, N is the total number of the pixels within the breast, $\mu_{ref,i}$ is the value of the i-th pixel in the reference FDK image, and $\mu_{FIRST,i}$ is the value of the i-th pixel in the FIRST image. RMSE was calculated as:

$$RMSE = \sqrt{\frac{1}{N}\sum_{i=1}^{N}\left(\mu_{ref,i} - \mu_{FIRST,i}\right)^2} \quad (3)$$

Computation of bias and RMSE used the entire breast volume, except for the region closest to the chest-wall due to irregular breast shapes contributing to inaccurate identification of skin (Shi *et al.*, 2013) for generating the image masks, and due to beam hardening artifacts from the breast support insert present in the cone-beam breast CT system.

2.E. Statistical analysis

All image quality metrics considered in the study were continuous variables and were tested for normality assumption (Shapiro-Wilks test). Depending upon whether the normality assumption was satisfied, either generalized linear models (repeated measures analysis of variance) or its non-parametric equivalent, Friedman's test, was used to determine if each image quality metric differed between the reconstructions. If the metrics different among reconstructions, follow-up pairwise analyses were conducted with multiple-comparisons (Tukey-Kramer) adjustment. Effects associated with $p<0.05$ were considered significant. Image quality metrics computed with the full-scan FDK reconstruction as the reference (bias and RMSE) were tested to determine if they differed from zero (one sample t-test or one sample median test, depending on normal distribution). All analyses were performed using statistical software (SAS® version 9.4, SAS Institute Inc., Cary, NC).

3. RESULTS

The results from the initial investigations on the forward/backward projection methods and the appropriateness of the number of iterations are presented first, followed by the image quality evaluation of the various short-scan, sparse-view reconstructions. In order to assist in visual analyses, a representative case for each of small, medium and large breasts are shown. The diameter of the breast at the chest wall were 9.71, 13.95, and 15.73 cm, respectively, for the small, medium and large breasts. The same set of cases are shown for consistency. All images shown are 5 slice average centered about the calcified lesion and is consistent

with standard clinical interpretation, which uses a scrolling/moving average of 5 or 10 slices. All images are prior to transformation to Hounsfield Units (HU) and hence are in units of linear attenuation coefficient (cm^{-1}). A consistent display window of [0.15, 0.35] cm^{-1} is used throughout the manuscript.

3.A. Voxel, ray and distance-driven methods

The results from voxel, ray, and distance-driven forward/back projection methods implemented with FIRST algorithm using full-scan dataset (300 views; 360°) are shown in Fig 5 for the representative cases of small, medium, and large breasts. For different breast sizes, no discernible artifacts or differences were observed among these methods. The reconstruction time with GPU implementation (Quadro P6000, NVidia Corporation, Santa Clara, CA) for an example case of large breast is summarized in Table 2. The reported reconstruction time is normalized to per slice and per iteration. The reconstruction time of the ray-driven method was slightly faster than the voxel-driven and substantially faster than the distance-driven approaches. Hence, the ray-driven method was used hereon throughout the study for both forward projection and back projection steps to accelerate the image reconstruction process.

3.B. Convergence analysis

Defining ϵ as the l_2 distance between the estimated sinogram $\tilde{g}$, and the acquired or measured sinogram, g_{data}, the FIRST algorithm seeks a solution to satisfy the following equations (Sidky and Pan, 2008),

$$\vec{\tilde{f}} = Argument_{min} \left\| \vec{f} \right\|_{TV} \tag{4}$$

$$|\tilde{g} - g_{data}| \leq \epsilon \tag{5}$$

$$\vec{f} \geq 0, \tag{6}$$

Equation (4) is the constrained TV minimization, the equation (5) is the data-consistency constraint, and the equation (6) is the enforcement of non-negativity. The ϵ is the parameter used for optimization process, and it is also indicated as a bound of the error between the estimated projections and the true projections. Ideally, ϵ should be zero when the number of iterations is infinity. However, it is not practical to have infinite number of iterations. Therefore, we devised a relaxed convergence condition of $\epsilon \leq 10^{-4}$ that is consistent with prior literature (Bian *et al.*, 2014).

Hyper-parameters used in our previous study (Tseng *et al.*, 2020) were based on full-scan and non-sparse-view data sets, i.e. complete data sets. We kept all hyper-parameters as in

the prior study except for the number of TV iterations. One each of large, medium, and small size breasts among the 30 cases were selected for optimizing the number of TV iterations. For each breast and sampling scheme, the number of TV iterations were varied and the ϵ values were calculated. Two methods (A and B) were used to determine the value of ϵ. Method A was based on visual assessment. This is illustrated for a large breast in Fig 6 for the short-scan trajectory with 225 views in 270°. When the number of TV iterations increase, the noise decreases (Fig 6b to 6f). However, the images appear blocky when the number of TV iterations is large (Fig 6b to 6d). On the other hand, the image looks noisy (Fig 6f) when the number of TV iterations is small. Two American Board of Radiology-certified diagnostic medical physicists with more than 20 years of experience in breast imaging reviewed the images. Visibility of microcalcifications and fine structures, noise, blocky or patchy background, and artifacts were considered for ranking the images. The median of the two medical physicist rankings was used to determine the best choice. For the example case, 15 TV iterations (Fig 6e) had the highest median ranking and provides a better balance based on visual analysis.

Method B was suggested by Bian et. al (Bian *et al.*, 2014) and uses the area under the image power spectrum (AUP). Representing the power spectrum as $P(k)$, where k is the spatial frequency, we have empirically shown (Vedantham *et al.*, 2012b) that the anatomical structures are dominant at $0.1 \leq k \leq 0.5$ cycles/mm. The system noise content, measured with homogenous phantoms, dominate at $k > 0.5$ cycles/mm (Benitez *et al.*, 2009). Two AUP values (Ap and Bp) were calculated. Ap is the AUP, where $0.1 \leq k \leq 0.5$ cycles/mm. Bp is the AUP, where $k > 0.5$ cycles/mm. Varying the number of TV iterations, Ap, Bp and ϵ were obtained, from which the derivative of AUP (Ap and Bp) with respect to ϵ decreases. Hence, in Fig 7, the higher values of ϵ are to the left in x-axis. The derivative of Ap (red were computed and plotted Fig 7. Please note that as the number of TV iterations increase, the ϵ dashed curve) is near zero when ϵ is smaller than the threshold ϵ_p, indicating that there is no change in terms of anatomical structure with increasing the number of TV iterations. However, the derivative of Bp (blue dashed curve) still increases, which implies that the changes in noise continues beyond ϵ_p. In this example case, the number of TV iterations associated with the ϵ that was just larger than ϵ_p is 15 and this is consistent with our visualization method.

The aforementioned two methods were performed for all short-scan and sparse-view trajectories with representative cases of large, medium, and small breasts. The two methods were consistent in identifying the optimal number of TV iterations (Table 3). We also investigated the effect of number of OS-SART iterations. We did not observe a difference in the images after 80 and 100 iterations of the FIRST algorithm using full-scan dataset (300 views; 360°) for the small, medium, and large breasts (Fig 8).

3.C. Qualitative evaluation

Figures 9 through 11 show the three orthogonal planes from all four short-scan, sparse-view reconstructions using the FIRST algorithm for the small, medium and large breasts, respectively. The reference full-scan FDK scan is also included in each figure and the calcified lesion is marked by an arrow. In each figure, the top, middle and bottom rows

correspond to coronal, axial and sagittal planes, respectively. The three orthogonal planes are shown to allow for visual analysis of artifacts, if present. In each figure, the columns from left to right are: reference FDK reconstruction with full-scan dataset (300 views; 360°), short-scan FIRST reconstructions arranged by number of views, *viz.*, 225 views in 270°, 180 views in 270°, 170 views in 204° and 168 views in 270°. In each panel, the reconstructed image is cropped to encompass the entire breast. Beam hardening artifacts from the breast support insert can be observed at slices close to the chest wall in axial and sagittal images. No scatter correction techniques (Shi *et al.*, 2016, 2017, 2018) were employed, resulting in cupping artifacts (darker shading) near the center of the breast that is better visualized in the coronal views (top row). Visually, the images from FIRST reconstructions are similar to the corresponding reference full-scan (300 views; 360°) FDK reconstruction (left column), even when the number of projections is reduced to 168 views (right column). With the FIRST reconstructions, there is a reduction in graininess in the image and there do not appear to be any additional artifacts. However, for the 180 views in 270° and 168 views in 270°, both of which use non-uniform sampling, there is some degradation of image quality, which is more noticeable in sagittal views in Fig 9. Assuming the AGD to the breast scales linearly with the number of views, this translates to approximately 56% of the dose from full-scan FDK reconstruction.

3. D. Visualization of microcalcifications

While figures 9 through 11 show the entire breast, it is difficult to assess the calcifications. Hence, figure 12 shows the zoomed-in view of the calcifications within the small, medium and large breasts. For brevity, only the cross-sectional slice corresponding to the coronal plane is shown. Visually, the conspicuity of calcifications with short-scan, sparse-view FIRST reconstructions appear similar to the reference full-scan FDK reconstruction. With FIRST reconstructions, reduction in background noise (graininess) is readily apparent. Qualitatively, the four short-scan reconstructions appear similar. However, near the vicinity of the calcification there appears a slight increase in beam hardening artifacts for the sparse-view, short-scan reconstruction with 168 views in 270° (right column, Fig 12) for one of the cases, corresponding to a small breast (top row, Fig 12).

3. E. Quantitative results

The summary statistics are provided in Table 4. The AGD is also included in the table for completeness. The AGD was computed by linearly scaling the AGD (Vedantham *et al.*, 2013c) from the reference full-scan (300 views; 360°) by the number of views. None of the image quality metrics satisfied the normality assumption ($P<0.04$, Shapiro-Wilks test). Hence, the P-values from the non-parametric Freidman's test are reported in Table 4. For each image quality metric, there was a significant difference among all reconstructions ($P<0.0006$, Cochran-Mantel-Haenszel statistic). Since bias and RMSE were computed with respect to the reference FDK reconstruction, the reported p-values are from comparisons among the four short-scan FIRST reconstructions. For the remaining image quality metrics (SDNR, FWHM and variance), the reported p-values are from comparisons among the all five reconstructions including the reference full-scan FDK reconstruction.

3.E.1. Comparison with reference full-scan reconstruction—The median values of the bias metric in short-scan reconstructions, computed with the full-scan FDK as the reference, were very low (8.6×10^{-4} – 10.3×10^{-4} cm^{-1}), but not zero ($P<0.0001$, one-sample median test). Similarly, the RMSE (median) in each short-scan reconstruction was low (6.8×10^{-6} – 9.8×10^{-6} cm^{-1}), but not zero ($P<0.0001$, one-sample median test). The $FWHM_{ML}$ from each short-scan reconstruction did not differ significantly from the reference FDK reconstruction ($P>0.118$). The $FWHM_{SI}$ from each short-scan reconstruction did not differ significantly from the reference FDK reconstruction ($P>0.389$), except for the short-scan reconstruction with 168 views in 270°, which was marginally significant ($P=0.046$). The SDNR and the variance from each short-scan reconstruction were significantly different from the reference full-scan FDK reconstruction ($P<0.0001$).

3.E.2. Comparisons among short-scan reconstructions—Fig 13 shows the box plot of the image quality metrics from short-scan reconstructions. For each metric, the best performance is achieved with 225 views in 270°. The SDNR decreases as the number of views are reduced and this is due to progressive increase in variance. In terms of bias, RMSE and FWHM, 170 views in 204°, which has the same angular interval (1.2° equiangular) as 225 views in 270°, performed better than 180 and 168 views in 270°. This suggests that the sampling interval is also an important consideration. It is relevant to note that 180 and 168 views in 270° used non-uniform sampling.

In pairwise comparisons, all pairs of short-scan reconstructions significantly differed ($P<0.0001$) in both RMSE and bias, with 225 views in 270° providing the lowest values, followed by 170 views in 204°, 180 views in 270° and 168 views in 270°. The $FWHM_{ML}$ did not differ significantly between the 180 and 168 views (in 270°) reconstructions ($P=0.911$), but differed ($P<0.047$) for all other pairs of short-scan reconstructions. Pairwise comparisons of $FWHM_{SI}$ from 225 views in 270° did not differ from other short-scan reconstructions ($P>0.06$). All other pairwise comparisons significantly differed in $FWHM_{SI}$ ($P<0.006$). In terms of SDNR, all pairs of short-scan reconstructions significantly differed ($P<0.0001$). The variance significantly differed among each pair of short-scan reconstructions ($P<0.031$), except between 170 views in 204° and 180 views in 270° ($P=0.083$).

A radar chart (Fig 14) is helpful in visualizing the trade-offs in image quality metrics among the four short-scan reconstructions. For each image quality metric, the mean rating from the sample size of n=30 subjects (cases) is used to construct the chart for each short-scan reconstruction. The best performance, which corresponds to the lowest bias, variance, FWHM and RMSE, and the highest SDNR, is assigned a rating of 1, and a rating of 4 corresponds to the worst performance among the four short-scan reconstructions. Overall, 225 views in 270° provided the best performance. Although the mean rating for $FWHM_{SI}$ appears worse with 225 views in 270°, it is relevant to note that this was not significantly different ($P=0.359$) from 170 views in 204°, which had the highest rating. Also, it is clear that 168 views in 270° provided the worst performance, among the conditions considered. Comparing 170 views in 204° with 180 views in 270°, all of the image quality metrics with the exception of variance and SDNR were better with 170 views in 204°. The reduced variance and consequently the increase in SDNR observed with the 180 views in 270°

short-scan can be attributed to the increased number of views (180 vs 170). These additional 10 views contribute to approximately 6% increase in AGD compared to 170 views. In summary, the analyses indicate the following: In terms of RMSE and bias, the rank order from best-to-worst is: 225 views in 270°; 170 views in 204°; 180 views in 270° and 168 views in 270°. In terms of FWHM, the rank order is: 225 views in 270° and 170 views in 204° (tie, not statistically different), followed by, 180 views in 270° and 168 views in 270°.

4. DISUCSSION

Referring to Table 4, the observed bias (median) values in short-scan reconstructions of 8.6×10^{-4} cm^{-1} to 10.3×10^{-4} cm^{-1} are approximately equivalent to 0.9–1.0 HU. In comparison, the noise in the reference full-scan FDK reconstruction, computed as the square-root of the variance is 7.7×10^{-3} cm^{-1}, is approximately one magnitude higher. Thus, the observation that the bias values in short-scan reconstructions differed from zero could be due to the noise in the full-scan FDK reconstruction, which was used as the reference for these computations. A similar observation can also be made for RMSE. It is also relevant to note that we chose the largest calcification in the breast for computing the FWHM, in order to improve reliability.

The full-scan data (300 views) were collected with uniform angular sampling (1.2°) in 360°. The short-scan and sparse-view data, in this study, were retrospectively taken from these full-scan datasets. Thus, angular sampling was uniform (1.2°) in some cases (225 views in 270° and 170 views in 204°) and was periodically non-uniform or quasi-uniform (1.2°/2.4°) in the other two cases (180 and 168 views in 270-degree). Although Jorgensen and Sidky(Jorgensen and Sidky, 2015) suggested to use uniform angular sampling for full-scan (360°) sparse-view acquisition in compressed sensing techniques, but remains a question for short-scan acquisition. This study was not designed to address this question, due to the retrospective use of clinical datasets with predefined angular sampling interval.

Regarding the AGD for short-scan trajectories, this was computed by linearly scaling the AGD from full-scan acquisition (300 views; 360°) by the number of views. This assumes that the radiation dose per view is uniform. While the tube current (mA) per projection was maintained constant throughout the acquisition for each breast, this assumption is strictly valid only if the breast is aligned with the axis of rotation and the breast is symmetric about the axis of rotation. Thus the AGD reported is an approximation. Investigation into the effects of breast positioning and breast shape in short-scan trajectory on AGD and the dose distribution is subject of ongoing research and will be reported in future. The scan time for the US FDA approved breast CT system is 10 seconds and is primarily due to the limited frame rate (30 frames/second) of the detector used in the system. The reduction in the number of views in conjunction with faster frame-rate detectors that are available could substantially reduce scan time such that it is comparable to digital breast tomosynthesis (Vedantham *et al.*, 2015a).

Importantly, this study demonstrates that the angular range considered for the short-scan trajectory can provide for artifact-free images with substantial reduction in image noise and

without loss of spatial resolution. Implementing a short-scan trajectory in a prone breast CT system is relatively simple.

In summary, we have investigated the potential of short-scan, sparse-view reconstruction for use in dedicated cone-beam breast CT system using a highly-accelerated variant of ASD-POCS, referred to as FIRST reconstruction (Tseng *et al.*, 2020). The short-scan reconstructions were visually similar to full-scan FDK reconstruction with substantial noise reduction, in spite of fewer projection views. Quantitative analyses verified these visual observations with a noticeable reduction in variance, which contributed to a significant improvement in SDNR. It was also shown that the method did not increase bias or RMSE, and the spatial resolution was similar to full-scan FDK reconstruction.

Evaluation of the quality of images generated by these alternative reconstruction techniques is important. In addition to metrics such as bias, noise (variance), SDNR, and spatial resolution (FWHM), task-specific evaluation is important. Optimally, such image quality assessment should be measured by an observer based upon clinically relevant tasks such as the detection of the lesion or estimating the tumor volume. However, at this early design stage, it is more efficient and cost-effective to analyze the image quality that is achievable using standard or conventional image quality metrics, such as those used in this study, prior to conducting a reader study. The focus of this study is to identify the radiation dose range which could give us reasonable and acceptable image quality with short-scan, sparse-view image reconstruction using FIRST algorithm, before proceeding to a reader study. An alternative approach using deep-learning (Fu *et al.*, 2019) based sparse-view reconstruction is also potentially feasible and is the subject of ongoing research.

5. CONCLUSIONS

We have demonstrated the feasibility of short-scan, sparse-view reconstruction using FIRST algorithm in clinical breast CT datasets. Artifact-free reconstructions with substantial reduction in image noise and without loss of spatial resolution is feasible with short-scan trajectories covering an angular range of 204° to 270°. Results from quantitative analysis show the ability to achieve improved performance with short-scan FIRST reconstruction compared to full-scan FDK reconstruction. The study shows that when the angular sampling interval is maintained constant, increasing the angular range which results in more number of views, provided better quantitative results; but, at the cost of increased radiation dose. Within the constraints of the available clinical datasets, 225 views in 270° performed the best, followed by 170 views in 204°, in terms of quantitative metrics. It is relevant to note that both these trajectories used uniform angular sampling. These results also demonstrate the potential for compressed sensing based image reconstruction algorithms to yield better image quality, even when the number of views is substantially reduced. The fewer number of views allows for substantial reduction in radiation dose to the breast and scan time, which enables the potential clinical use of breast CT in a screening environment and could greatly accelerate its clinical adoption.

ACKNOWLEDGEMENTS

This work was supported in part by the National Cancer Institute (NCI) of the National Institutes of Health (NIH) grants R21 CA134128, R01 CA195512, R01 CA199044 and R01 CA241709. The contents are solely the responsibility of the authors and do not represent the official views of the NCI or the NIH.

REFERENCES

Aminololama-Shakeri S, Abbey CK, Lopez JE, Hernandez AM, Gazi P, Boone JM and Lindfors KK 2019 Conspicuity of suspicious breast lesions on contrast enhanced breast CT compared to digital breast tomosynthesis and mammography Br J Radiol 92 20181034. 10.1259/bjr.20181034 [PubMed: 30810339]

Benitez RB, Ning R, Conover D and Liu S 2009 NPS characterization and evaluation of a cone beam CT breast imaging system J Xray Sci Technol 17 17–40. 10.3233/XST-2009-0213 [PubMed: 19644211]

Bian J, Siewerdsen JH, Han X, Sidky EY, Prince JL, Pelizzari CA and Pan X 2010 Evaluation of sparse-view reconstruction from flat-panel-detector cone-beam CT Phys Med Biol 55 6575–99. 10.1088/0031-9155/55/22/001 [PubMed: 20962368]

Bian J, Yang K, Boone JM, Han X, Sidky EY and Pan X 2014 Investigation of iterative image reconstruction in low-dose breast CT Phys Med Biol 59 2659–85. 10.1088/0031-9155/59/11/2659 [PubMed: 24786683]

Biguri A 2018 Iterative Reconstruction and Motion compensation in Computed Tomography on GPUs. In: Department of Electronic & Electrical Engineering, Doctoral (PhD) Thesis, (Bath, UK: University of Bath)

Biguri A, Dosanjh M, Hancock S and Soleimani M 2016 TIGRE: a MATLAB-GPU toolbox for CBCT image reconstruction Biomed Phys Eng Expr 2 055010. 10.1088/2057-1976/2/5/055010

Candes EJ, Romberg JK and Tao T 2006 Stable signal recovery from incomplete and inaccurate measurements Commun Pur Appl Math 59 1207–23. 10.1002/cpa.20124

Candes EJ and Tao T 2006 Near-Optimal Signal Recovery From Random Projections: Universal Encoding Strategies? Ieee T Inform Theory 52 5406–25. 10.1109/tit.2006.885507

Chambolle A 2004 An algorithm for total variation minimization and applications J Math Imaging Vis 20 89–97. 10.1023/B:JMIV.0000011325.36760.1e

Chen L, Abbey CK and Boone JM 2013 Association between power law coefficients of the anatomical noise power spectrum and lesion detectability in breast imaging modalities Phys Med Biol 58 1663–81. 10.1088/0031-9155/58/6/1663 [PubMed: 23422272]

Chen L, Boone JM, Abbey CK, Hargreaves J, Bateni C, Lindfors KK, Yang K, Nosratieh A, Hernandez A and Gazi P 2015 Simulated lesion, human observer performance comparison between thin-section dedicated breast CT images versus computed thick-section simulated projection images of the breast Phys Med Biol 60 3347–58. 10.1088/0031-9155/60/8/3347 [PubMed: 25825980]

Cole EB, Campbell AS, Vedantham S, Pisano ED and Karellas A 2015 Clinical Performance of Dedicated Breast Computed Tomography in Comparison to Diagnostic Digital Mammography [abstract # SSA01–09]. In: 101st Scientific Assembly and Annual Meeting of the Radiological Society of North America (RSNA 2015), (Chicago, IL: Radiology Society of North America) archive.rsna.org/2015/15006483.html

Feldkamp LA, Davis LC and Kress JW 1984 Practical Cone-Beam Algorithm Journal of the Optical Society of America a-Optics Image Science and Vision 1 612–9. 10.1364/Josaa.1.000612

Friedewald SM, Rafferty EA, Rose SL, Durand MA, Plecha DM, Greenberg JS, Hayes MK, Copit DS, Carlson KL, Cink TM, Barke LD, Greer LN, Miller DP and Conant EF 2014 Breast cancer screening using tomosynthesis in combination with digital mammography JAMA 311 2499–507. 10.1001/jama.2014.6095 [PubMed: 25058084]

Fu Z, Tseng HW, Vedantham S, Karellas A and Bilgin A 2019 Deep Learning-Driven Sparse-View Reconstruction for Radiation Dose Reduction in Dedicated Breast CT: Quantitative Evaluation [abstract # SSC13–05]. In: Radiological Society of North America 2019 Scientific Assembly and

Annual Meeting, (Chicago, IL: Radiological Society of North America (RSNA)) archive.rsna.org/2019/19011467.html

Gordon R, Bender R and Herman GT 1970 Algebraic reconstruction techniques (ART) for three-dimensional electron microscopy and x-ray photography J Theor Biol 29 471–81. 10.1016/0022-5193(70)90109-8 [PubMed: 5492997]

Gregor J and Fessler JA 2015 Comparison of SIRT and SQS for Regularized Weighted Least Squares Image Reconstruction IEEE Trans Comput Imaging 1 44–55. 10.1109/TCI.2015.2442511 [PubMed: 26478906]

Hernandez AM, Abbey CK, Ghazi P, Burkett G and Boone JM 2020 Effects of kV, filtration, dose, and object size on soft tissue and iodine contrast in dedicated breast CT Med Phys 10.1002/mp.14159

Jorgensen JS and Sidky EY 2015 How little data is enough? Phase-diagram analysis of sparsity-regularized X-ray computed tomography Philosophical transactions. Series A, Mathematical, physical, and engineering sciences 373 10.1098/rsta.2014.0387

Lindfors KK, Boone JM, Nelson TR, Yang K, Kwan AL and Miller DF 2008 Dedicated breast CT: initial clinical experience Radiology 246 725–33. 10.1148/radiol.2463070410 [PubMed: 18195383]

Liu R, Fu L, De Man B and Yu H 2017 GPU-based Branchless Distance-Driven Projection and Backprojection IEEE Trans Comput Imaging 3 617–32. 10.1109/TCI.2017.2675705 [PubMed: 29333480]

Luck F, Kolditz D, Hupfer M and Kalender WA 2013 Effect of shaped filter design on dose and image quality in breast CT Phys Med Biol 58 4205–23. 10.1088/0031-9155/58/12/4205 [PubMed: 23715466]

Michaelsen KE, Krishnaswamy V, Shi L, Vedantham S, Poplack SP, Karellas A, Pogue BW and Paulsen KD 2015 Calibration and optimization of 3D digital breast tomosynthesis guided near infrared spectral tomography Biomedical optics express 6 4981–91. 10.1364/BOE.6.004981 [PubMed: 26713210]

Niklason LT, Christian BT, Niklason LE, Kopans DB, Castleberry DE, Opsahl-Ong BH, Landberg CE, Slanetz PJ, Giardino AA, Moore R, Albagli D, DeJule MC, Fitzgerald PF, Fobare DF, Giambattista BW, Kwasnick RF, Liu J, Lubowski SJ, Possin GE, Richotte JF, Wei CY and Wirth RF 1997 Digital tomosynthesis in breast imaging Radiology 205 399–406. 10.1148/radiology.205.2.9356620 [PubMed: 9356620]

O'Connell A, Conover DL, Zhang Y, Seifert P, Logan-Young W, Lin CF, Sahler L and Ning R 2010 Cone-beam CT for breast imaging: Radiation dose, breast coverage, and image quality AJR Am J Roentgenol 195 496–509. 10.2214/AJR.08.1017 [PubMed: 20651210]

O'Connell AM, Karellas A and Vedantham S 2014 The potential role of dedicated 3D breast CT as a diagnostic tool: review and early clinical examples Breast J 20 592–605. 10.1111/tbj.12327 [PubMed: 25199995]

O'Connell AM, Karellas A, Vedantham S and Kawakyu-O'Connor DT 2018 Newer Technologies in Breast Cancer Imaging: Dedicated Cone-Beam Breast Computed Tomography Seminars in ultrasound, CT, and MR 39 106–13. 10.1053/j.sult.2017.09.001 [PubMed: 29317032]

Parker DL 1982 Optimal short scan convolution reconstruction for fanbeam CT Med Phys 9 254–7. 10.1118/1.595078 [PubMed: 7087912]

Peters TM 1981 Algorithms for Fast Back- and Re-Projection in Computed Tomography IEEE Trans Nucl Sci 28 3641–7. 10.1109/TNS.1981.4331812

Pisano ED, Gatsonis C, Hendrick E, Yaffe M, Baum JK, Acharyya S, Conant EF, Fajardo LL, Bassett L, D'Orsi C, Jong R, Rebner M and Digital Mammographic Imaging Screening Trial Investigators G 2005 Diagnostic performance of digital versus film mammography for breast-cancer screening N Engl J Med 353 1773–83. 10.1056/NEJMoa052911 [PubMed: 16169887]

Prionas ND, Lindfors KK, Ray S, Huang SY, Beckett LA, Monsky WL and Boone JM 2010 Contrast-enhanced dedicated breast CT: initial clinical experience Radiology 256 714–23. 10.1148/radiol.10092311 [PubMed: 20720067]

Rudin LI, Osher S and Fatemi E 1992 Nonlinear Total Variation based noise removal algorithms Physica D 60 259–68. Doi 10.1016/0167-2789(92)90242-F

Sezan MI 1992 An overview of convex projections theory and its application to image recovery problems Ultramicroscopy 40 55–67. 10.1016/0304-3991(92)90234-B

Shi L, Vedantham S, Karellas A and O'Connell AM 2013 Skin thickness measurements using high-resolution flat-panel cone-beam dedicated breast CT Med Phys 40 031913. 10.1118/1.4793257 [PubMed: 23464328]

Shi L, Vedantham S, Karellas A and Zhu L 2016 Library based x-ray scatter correction for dedicated cone beam breast CT Med Phys 43 4529. 10.1118/1.4955121 [PubMed: 27487870]

Shi L, Vedantham S, Karellas A and Zhu L 2017 X-ray scatter correction for dedicated cone beam breast CT using a forward-projection model Med Phys 10.1002/mp.12213

Shi L, Vedantham S, Karellas A and Zhu L 2018 The role of off-focus radiation in scatter correction for dedicated cone beam breast CT Med Phys 45 191–201. 10.1002/mp.12686 [PubMed: 29159941]

Siddon RL 1985 Fast calculation of the exact radiological path for a three-dimensional CT array Med Phys 12 252–5. 10.1118/1.595715 [PubMed: 4000088]

Sidky EY and Pan X 2008 Image reconstruction in circular cone-beam computed tomography by constrained, total-variation minimization Phys Med Biol 53 4777–807. 10.1088/0031-9155/53/17/021 [PubMed: 18701771]

Strong D and Chan T 2003 Edge-preserving and scale-dependent properties of total variation regularization Inverse Problems 19 S165–S87. 10.1088/0266-5611/19/6/059

Sujlana PS, Mahesh M, Vedantham S, Harvey SC, Mullen LA and Woods RW 2018 Digital breast tomosynthesis: Image acquisition principles and artifacts Clinical imaging 10.1016/j.clinimag.2018.07.013

Suryanarayanan S, Karellas A, Vedantham S, Glick SJ, D'Orsi CJ, Baker SP and Webber RL 2000 Comparison of tomosynthesis methods used with digital mammography Acad Radiol 7 1085–97. 10.1016/s1076-6332(00)80061-6 [PubMed: 11131053]

Suryanarayanan S, Karellas A, Vedantham S, Ved H, Baker SP and D'Orsi CJ 2002 Flat-panel digital mammography system: contrast-detail comparison between screen-film radiographs and hard-copy images Radiology 225 801–7. 10.1148/radiol.2253011736 [PubMed: 12461264]

Tseng HW, Vedantham S and Karellas A 2020 Cone-beam breast computed tomography using ultra-fast image reconstruction with constrained, total-variation minimization for suppression of artifacts Phys Med 73 117–24. 10.1016/j.ejmp.2020.04.020 [PubMed: 32361156]

Tuy HK 1983 An Inversion-Formula for Cone-Beam Reconstruction SIAM Journal on Applied Mathematics 43 546–52. Doi 10.1137/0143035

Vedantham S and Karellas A 59th Annual Meeting of the American Association of Physicists in Medicine (AAPM 2017), (Denver, CO, 2017), vol. Series Medical Physics 44(6), 2017 AAPM Annual Meeting Program): American Association of Physicists in Medicine) p 3177.

Vedantham S, Karellas A, Emmons MM, Moss LJ, Hussain S and Baker SP 2013a Dedicated breast CT: geometric design considerations to maximize posterior breast coverage Phys Med Biol 58 4099–118. 10.1088/0031-9155/58/12/4099 [PubMed: 23685899]

Vedantham S, Karellas A, Suryanarayanan S, Albagli D, Han S, Tkaczyk EJ, Landberg CE, Opsahl-Ong B, Granfors PR, Levis I, D'Orsi CJ and Hendrick RE 2000a Full breast digital mammography with an amorphous silicon-based flat panel detector: physical characteristics of a clinical prototype Med Phys 27 558–67. 10.1118/1.598895 [PubMed: 10757607]

Vedantham S, Karellas A, Suryanarayanan S, D'Orsi CJ and Hendrick RE 2000b Breast imaging using an amorphous silicon-based full-field digital mammographic system: stability of a clinical prototype J Digit Imaging 13 191–9. 10.1007/BF03168394

Vedantham S, Karellas A, Vijayaraghavan GR and Kopans DB 2015a Digital Breast Tomosynthesis: State of the Art Radiology 277 663–84. 10.1148/radiol.2015141303 [PubMed: 26599926]

Vedantham S, O'Connell AM, Shi L, Karellas A, Huston AJ and Skinner KA 2014 Dedicated Breast CT: Feasibility for Monitoring Neoadjuvant Chemotherapy Treatment J Clin Imaging Sci 4 64. 10.4103/2156-7514.145867 [PubMed: 25558431]

Vedantham S, Shi L, Glick SJ and Karellas A 2013b Scaling-law for the energy dependence of anatomic power spectrum in dedicated breast CT Med Phys 40 011901. 10.1118/1.4769408 [PubMed: 23298092]

Vedantham S, Shi L and Karellas A 57th Annual Meeting of the American Association of Physicists in Medicine (AAPM), (Anaheim, CA, July 12–16, 2015 2015b), vol. Series Medical Physics 42–6. 2015 AAPM Annual Meeting Program) pp 3574–5.

Vedantham S, Shi L, Karellas A and O'Connell AM 2012a Dedicated breast CT: fibroglandular volume measurements in a diagnostic population Med Phys 39 7317–28. 10.1118/1.4765050 [PubMed: 23231281]

Vedantham S, Shi L, Karellas A, O'Connell AM and Conover D The Second International Conference on Image Formation in X-ray Computed Tomography, (Fort Douglas/Salt Lake City, UT. , June 24–27 2012b), vol. Series Proceedings of the 2nd International Conference on Image Formation in X-ray Computed Tomography) pp 70–3.

Vedantham S, Shi L, Karellas A, O'Connell AM and Conover DL 2013c Personalized estimates of radiation dose from dedicated breast CT in a diagnostic population and comparison with diagnostic mammography Phys Med Biol 58 7921–36. 10.1088/0031-9155/58/22/7921 [PubMed: 24165162]

Wang G and Jiang M 2004 Ordered-subset simultaneous algebraic reconstruction techniques (OS-SART) Journal of X-Ray Science and Technology 12 169–77.

Wesarg S, Ebert M and Bortfeld T 2002 Parker weights revisited Med Phys 29 372–8. 10.1118/1.1450132 [PubMed: 11929021]

Wright NC, Looker AC, Saag KG, Curtis JR, Delzell ES, Randall S and Dawson-Hughes B 2014 The Recent Prevalence of Osteoporosis and Low Bone Mass in the United States Based on Bone Mineral Density at the Femoral Neck or Lumbar Spine J Bone Miner Res 29 2520–6. 10.1002/jbmr.2269 [PubMed: 24771492]

Zbijewski W and Beekman FJ 2004 Characterization and suppression of edge and aliasing artefacts in iterative x-ray CT reconstruction Phys Med Biol 49 145–57. 10.1088/0031-9155/49/1/010 [PubMed: 14971778]

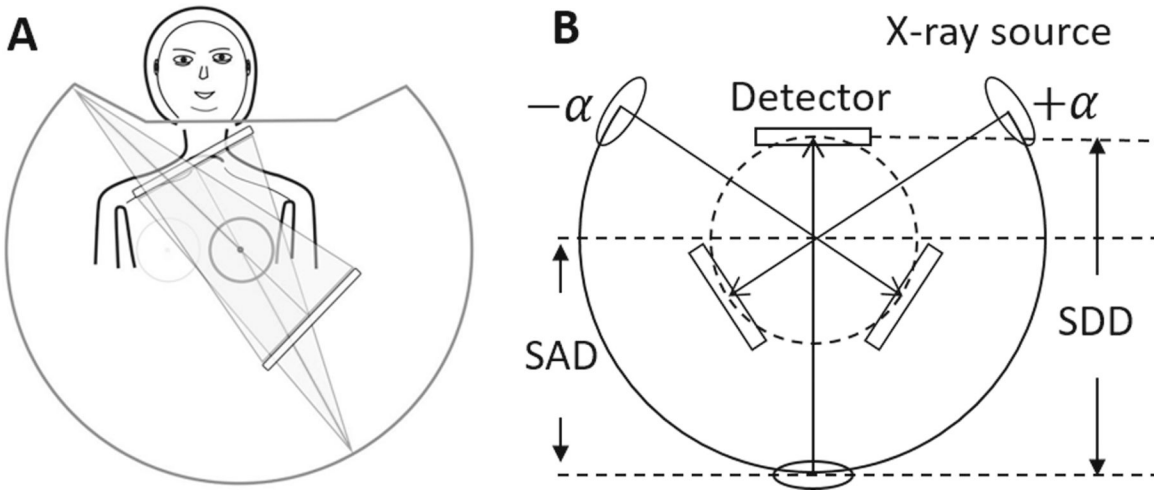

Fig1.

A: Schematic (anterior view) of short-scan, cone-beam breast CT system. B: Geometric parameters pertaining to system design. The x-ray source traverses an arc ($-\alpha$, $+\alpha$) inferior to the breast. SAD and SDD are the distances from the source to the axis-of-rotation and detector, respectively.

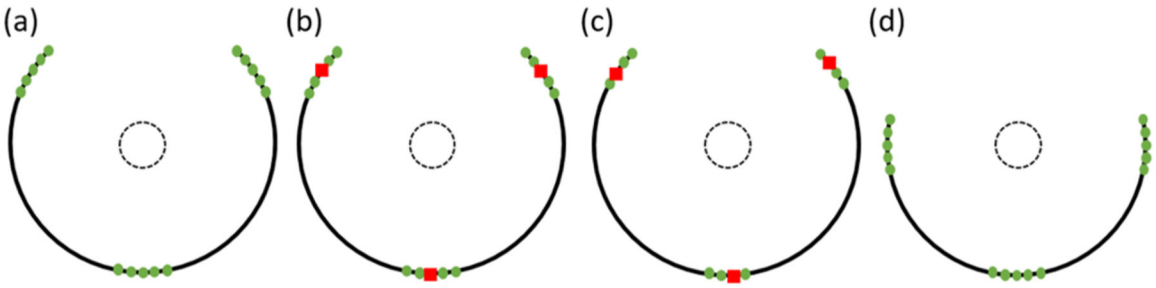

Fig 2.

Short-scan and sparse-view acquisitions schemes. The black curve presents the trajectory of the x-ray source. Projections corresponding to green circles were included and projections corresponding to red squares were excluded during image reconstruction. The dotted circle represents the imaged breast (not drawn to scale). (a) All 225 projections in 270° trajectory were selected, which results in uniform angular sampling. (b) 80% of 225 projections (the third projection was excluded in every five projections sub-group) were chosen, which results in 180 views over 270° trajectory with non-uniform angular sampling. (c) 75% of 225 projections (the third projection was excluded in every four projections sub-group) were chosen, resulting in 168 views over 270° trajectory with non-uniform angular sampling. (d) All 170 projections in 204° trajectory angle were used, resulting in uniform angular sampling.

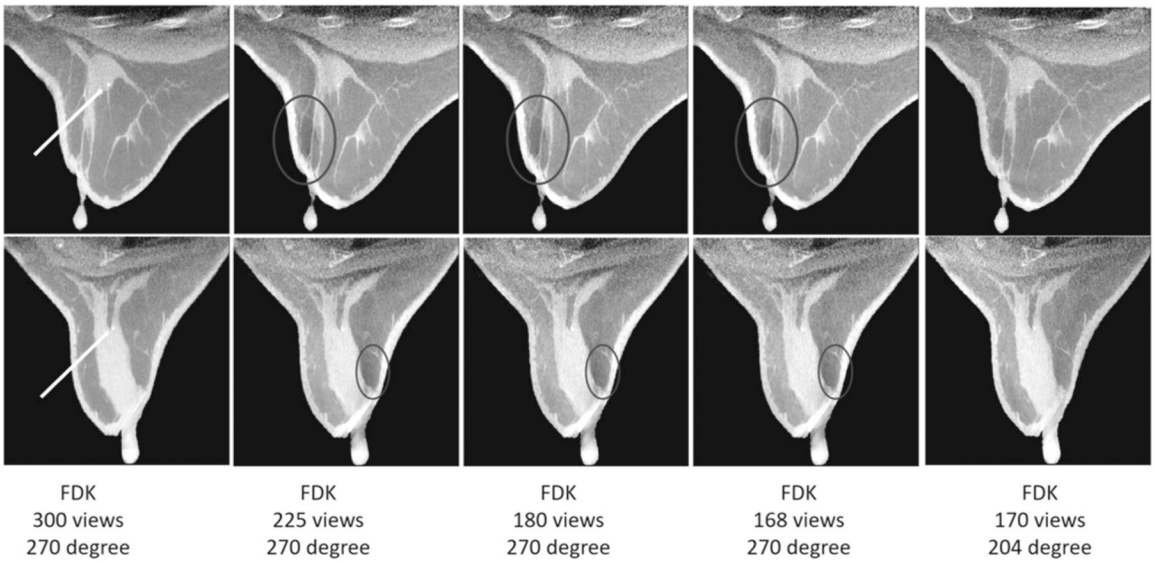

Fig 3.

Sagittal views (5-slice average) from FDK reconstructions. Left column is the reference full-scan FDK reconstruction. The arrows indicate the calcifications. The remaining 4 columns are short-scan FDK reconstructions with Parker weights. Circles mark the artifacts. The display window is [0.15 0.35] cm^{-1}.

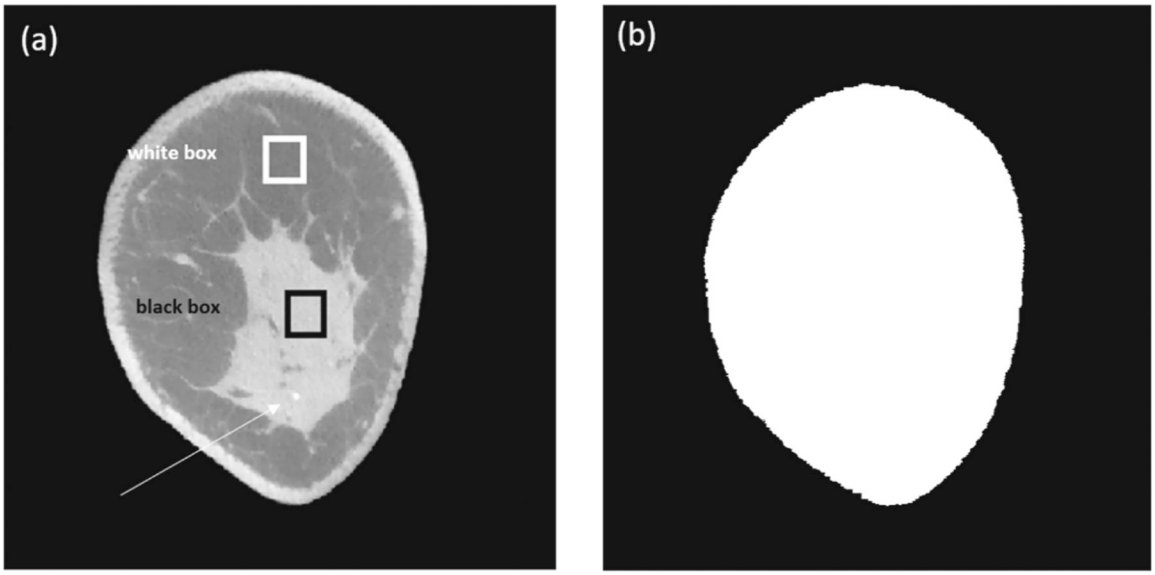

Fig 4.

(a) An example (single slice) showing the region-of-interest (ROI) for adipose (white box) and fibroglandular (black box) regions used to calculate noise and SDNR. A fixed ROI size of 32×32 pixels was used in all cases. The dynamic range is [0.15 0.35] cm^{-1}. The FWHM was calculated for the largest calcification in the cluster (arrow) along two orthogonal directions. (b) RMSE and bias were computed within the breast identified by the image mask corresponding to the slice in (a).

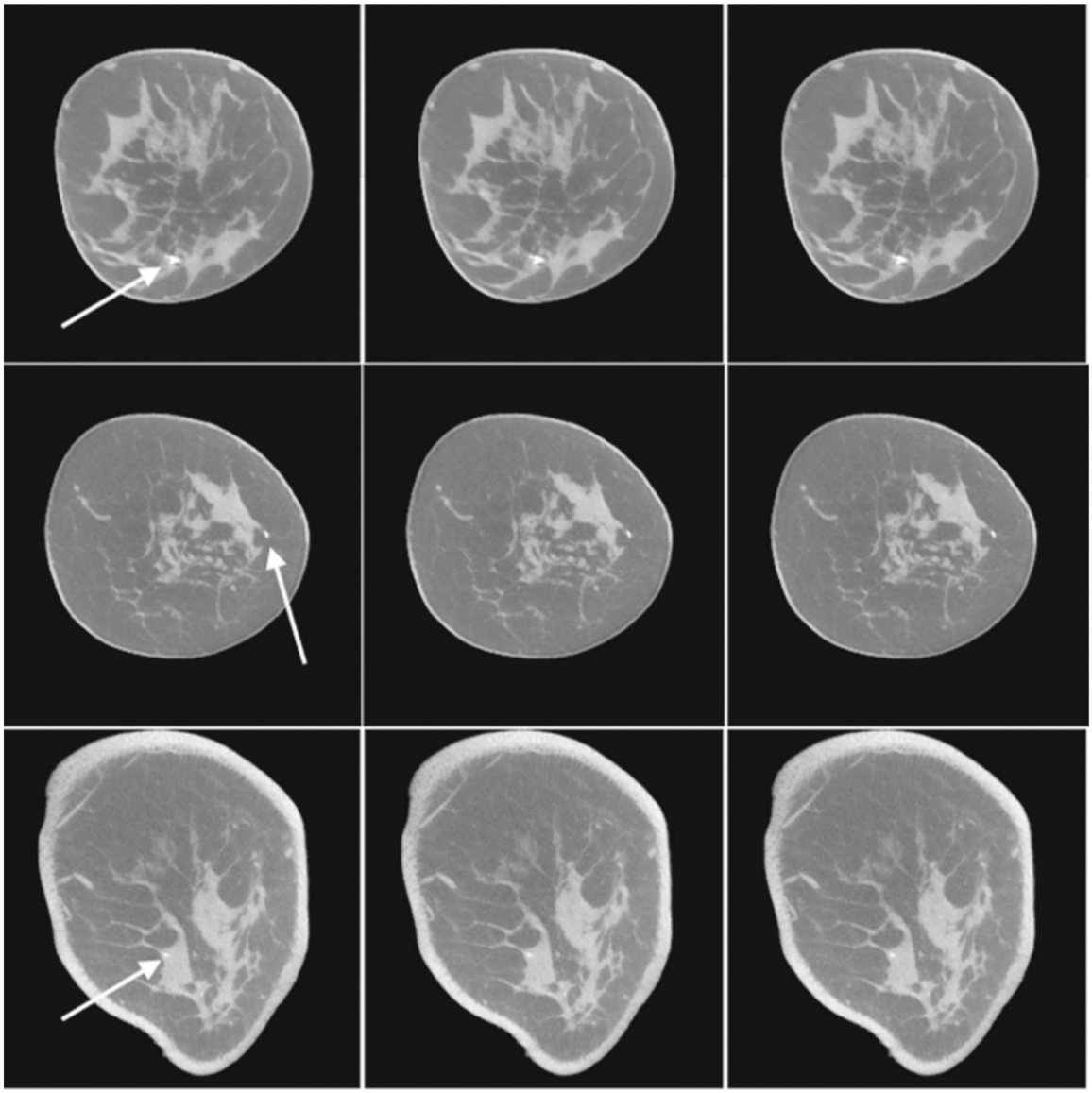

Fig 5.

Images (5-slice average) reconstructed by FIRST algorithm using different projection and back projection methods using full-scan dataset (300 views; 360°). The left, middle, and right columns are the images generated by the voxel-, ray-, and distance-driven methods, respectively. The top, middle, and bottom rows are the images of small-, medium-, and large-size breasts, respectively. The arrows indicate the calcifications. The display window is [0.15 0.35] cm^{-1}.

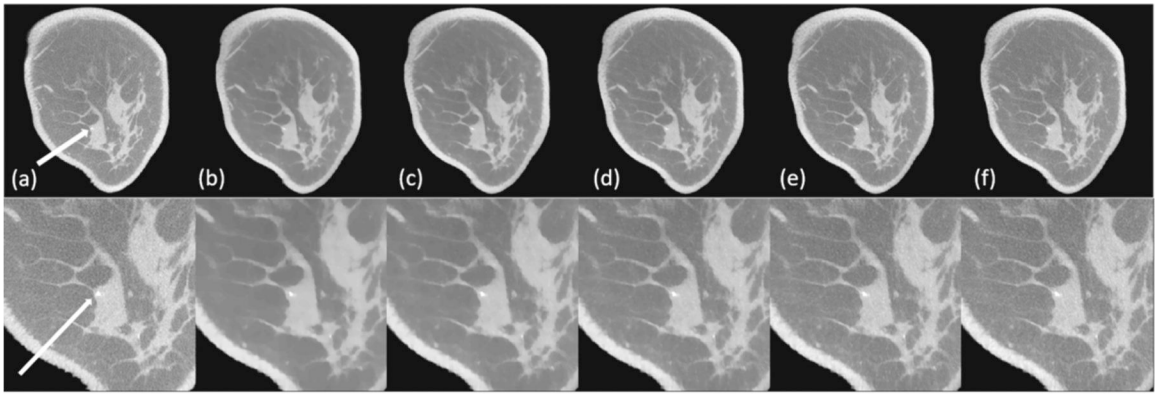

Fig 6.

Reconstructed Images (5-slice average). (a) Reference FDK full-scan (300 views in 360°) reconstruction. (b–f) FIRST reconstruction of short-scan trajectory (225 views in 270° with uniform sampling) with 30, 25, 20, 15 and 10 TV iterations, respectively. The bottom row shows the zoomed-in views. The arrows indicate the calcifications. The display window is [0.15 0.35] cm^{-1}.

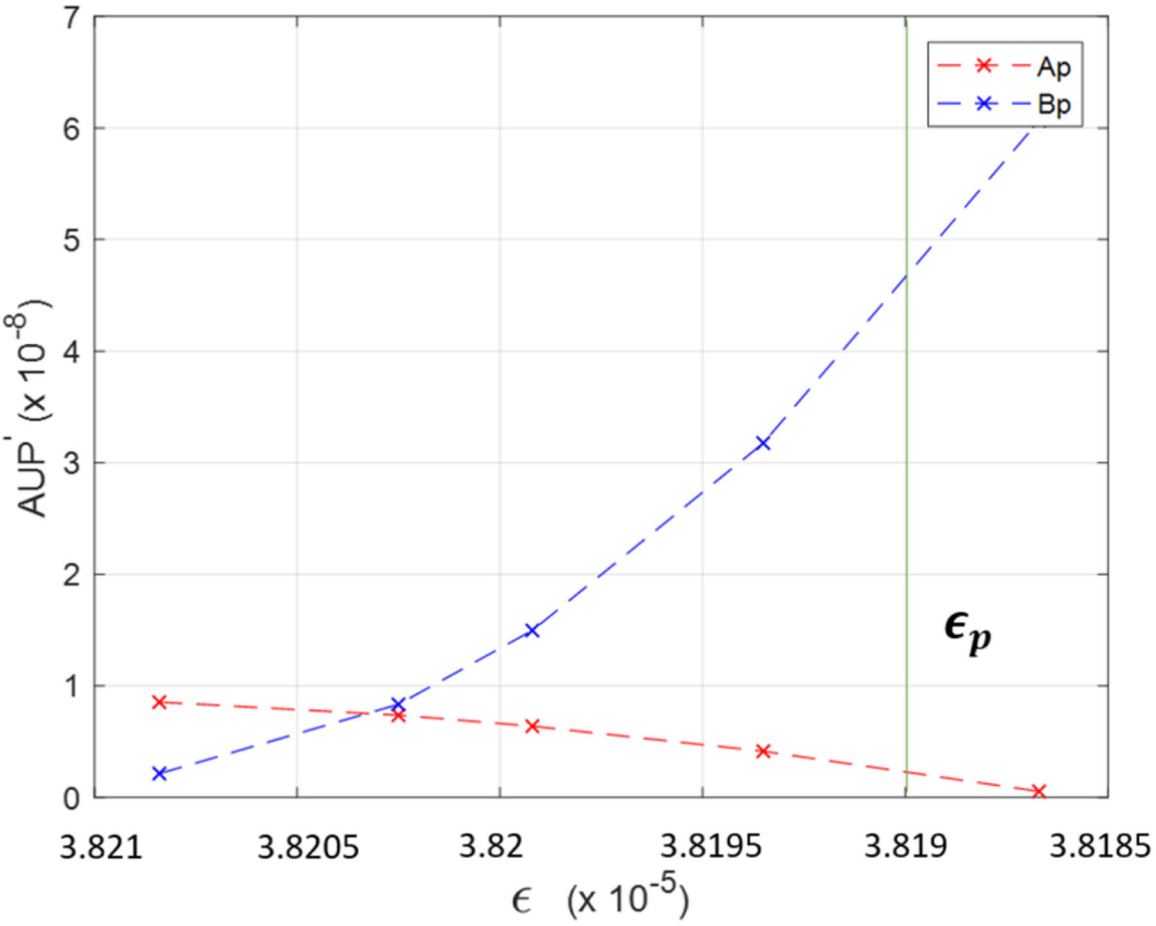

Fig 7.

The derivative of the area under the power spectrum (AUP) values (Ap and Bp) with respect to ϵ. The value of ϵ in the x-axis decreases from left to right. Ap is the AUP computed within the spatial frequency (k), $0.1 \leq k \leq 0.5$ cycles/mm. Bp is the AUP computed for $k >$ 0.5 cycles/mm.

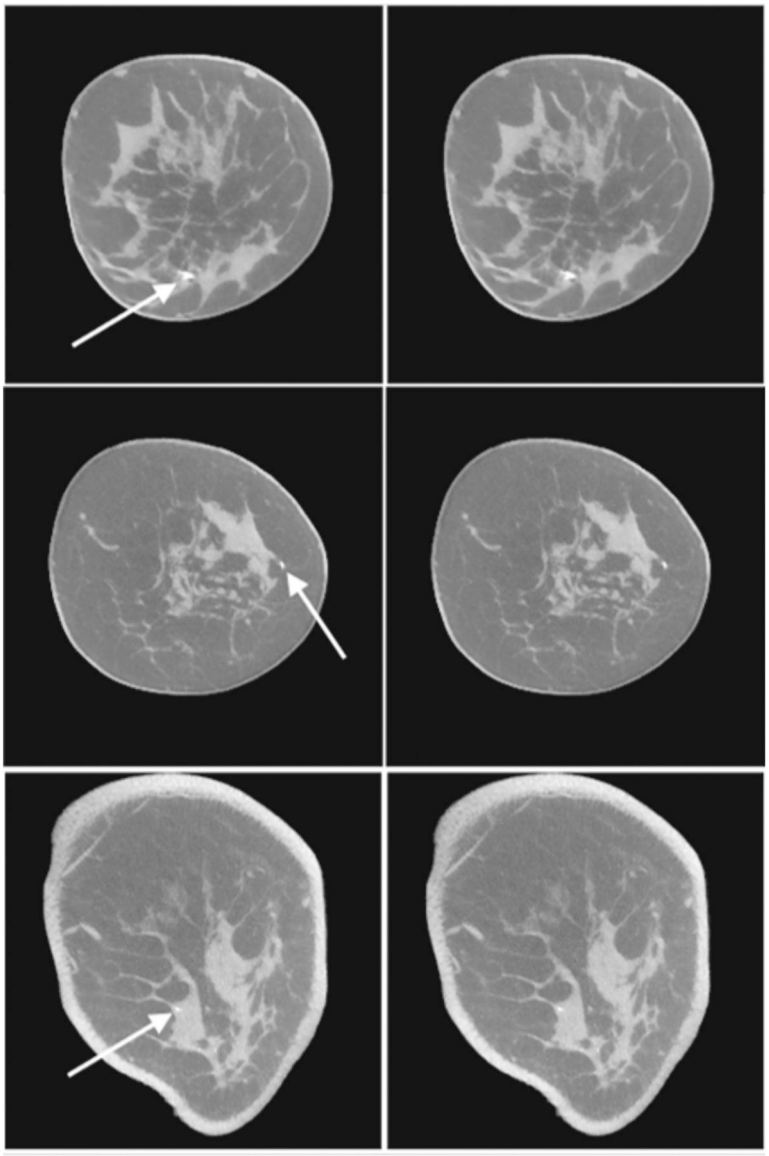

Fig 8.

Reconstructed images (5-slice average) after 80 and 100 iterations using FIRST algorithm with full-scan dataset (300 views; 360°). Images are processed by 5 slices average. The left and right column are the images generated by 80 and 100 iterations, respectively. The top, middle, and bottom row are the images of small-, medium-, and large-size breasts, respectively. The arrows indicate the calcifications. The display window is [0.15 0.35] cm^{-1}.

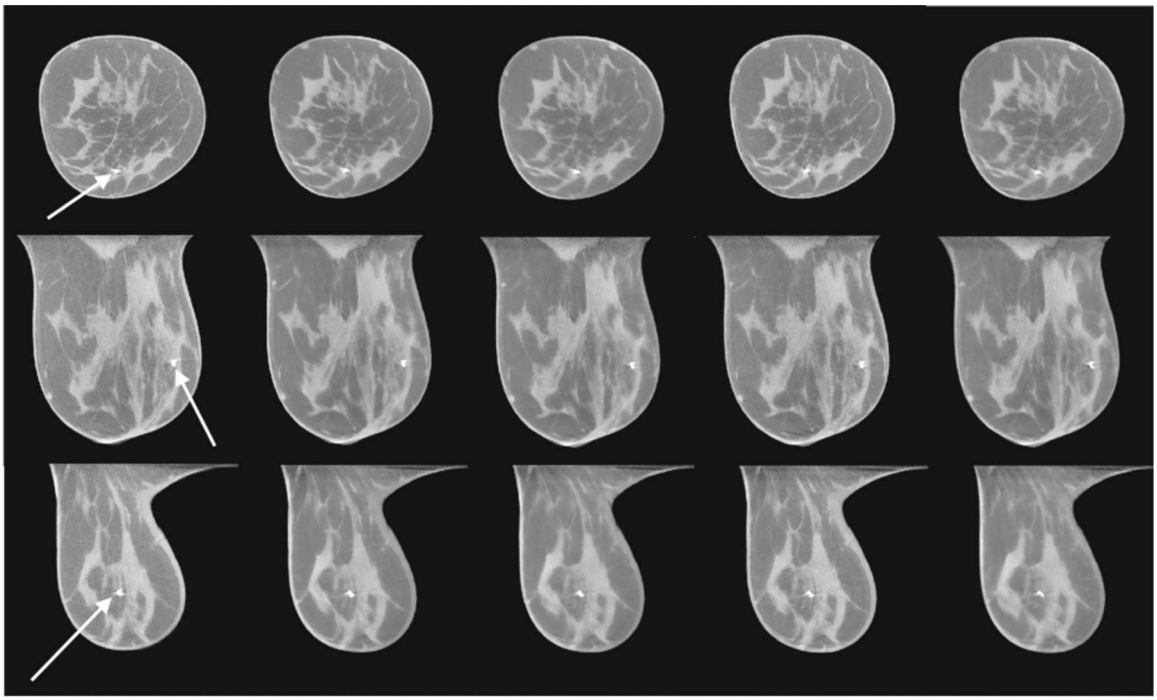

Fig 9.

Reconstructed images (5-slice average) of a small breast. The columns from left to right are the reference FDK (300 views; 360°), followed by short-scan FIRST reconstructions arranged by number views in descending order, viz., 225 views in 270°, 180 views in 270°, 170 views in 204° and 168 views in 270°. The top, middle and bottom rows correspond to coronal, axial and sagittal planes, respectively. The arrows mark the largest calcification, which was used for FWHM measurement. The display window is [0.15 0.35] cm^{-1}.

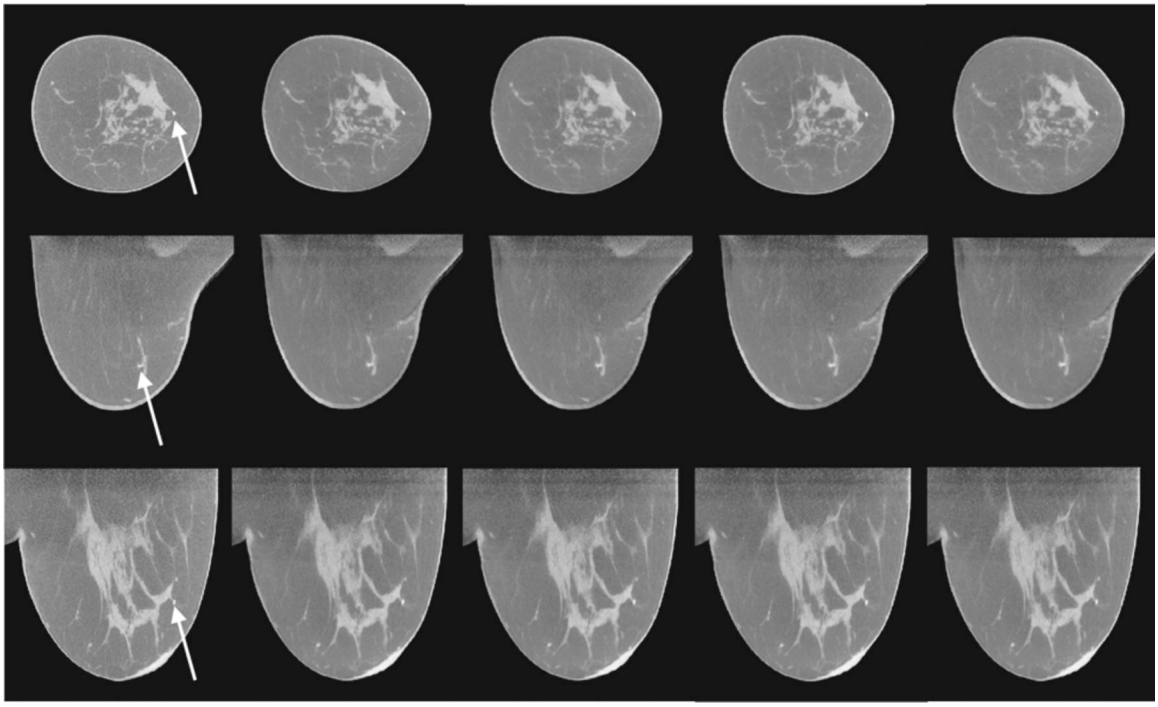

Fig 10.

Reconstructed images (5-slice average) of a medium breast. The columns from left to right are the reference FDK (300 views; 360°), followed by short-scan FIRST reconstructions arranged by number views in descending, viz., 225 views in 270°, 180 views in 270°, 170 views in 204° and 168 views in 270°. The top, middle and bottom rows correspond to coronal, axial and sagittal planes, respectively. The arrows mark the largest calcification, which was used for FWHM measurement. The display window is [0.15 0.35] cm^{-1}.

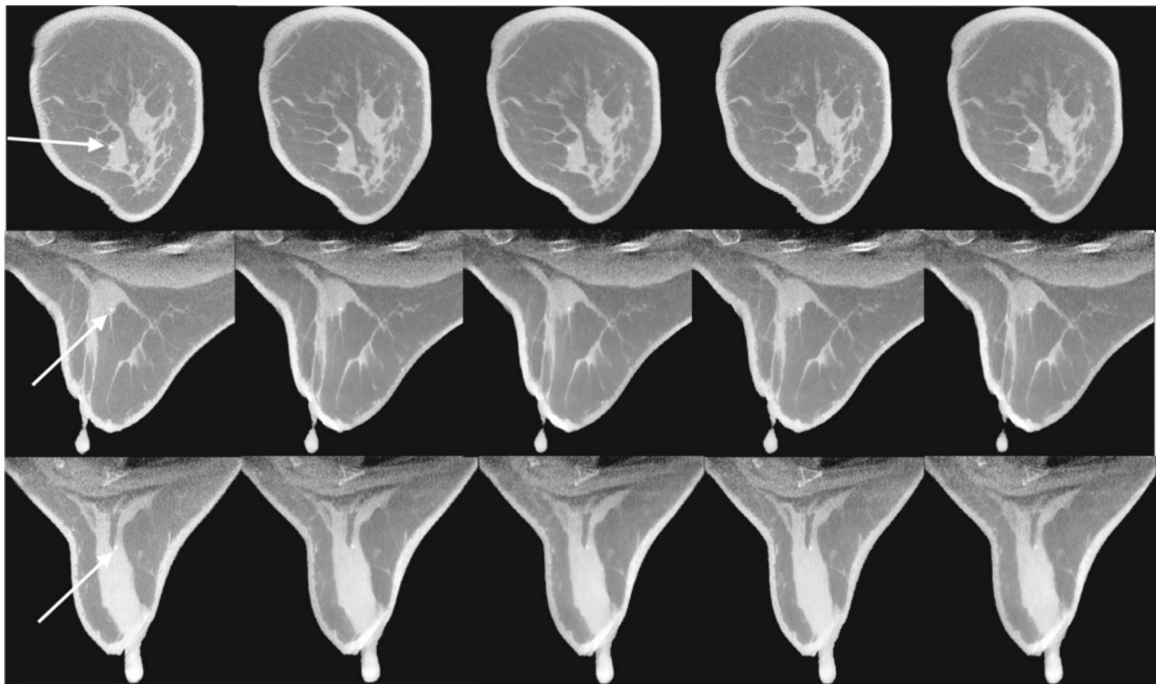

Fig. 11.

Reconstructed images (5-slice average) of a large breast. The columns from left to right are the reference FDK (300 views; 360°), followed by short-scan FIRST reconstructions arranged by number views in descending order, viz., 225 views in 270°, 180 views in 270°, 170 views in 204° and 168 views in 270°. The top, middle and bottom rows correspond to coronal, axial and sagittal planes, respectively. The arrows mark the largest calcification, which was used for FWHM measurement. The display window is [0.15 0.35] cm^{-1}.

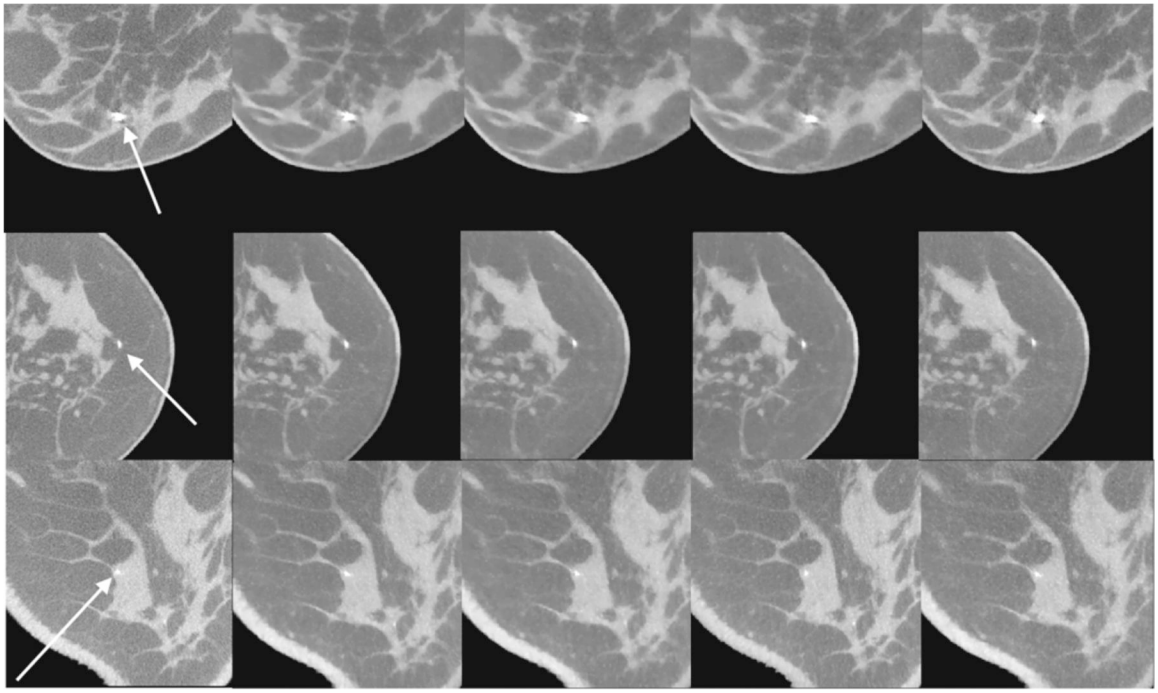

Fig 12.

Reconstructed images (5-slice average) with zoomed-in view of the calcifications. The columns from left to right are the reference FDK (300 views; 360°), followed by short-scan FIRST reconstructions arranged by number views in descending order, viz., 225 views in 270°, 180 views in 270°, 170 views in 204° and 168 views in 270°. The top, middle and bottom rows correspond to small, medium and large breasts, respectively. The arrows mark the largest calcification in each breast, which used for FWHM measurement. The display window is [0.15 0.35] cm^{-1}.

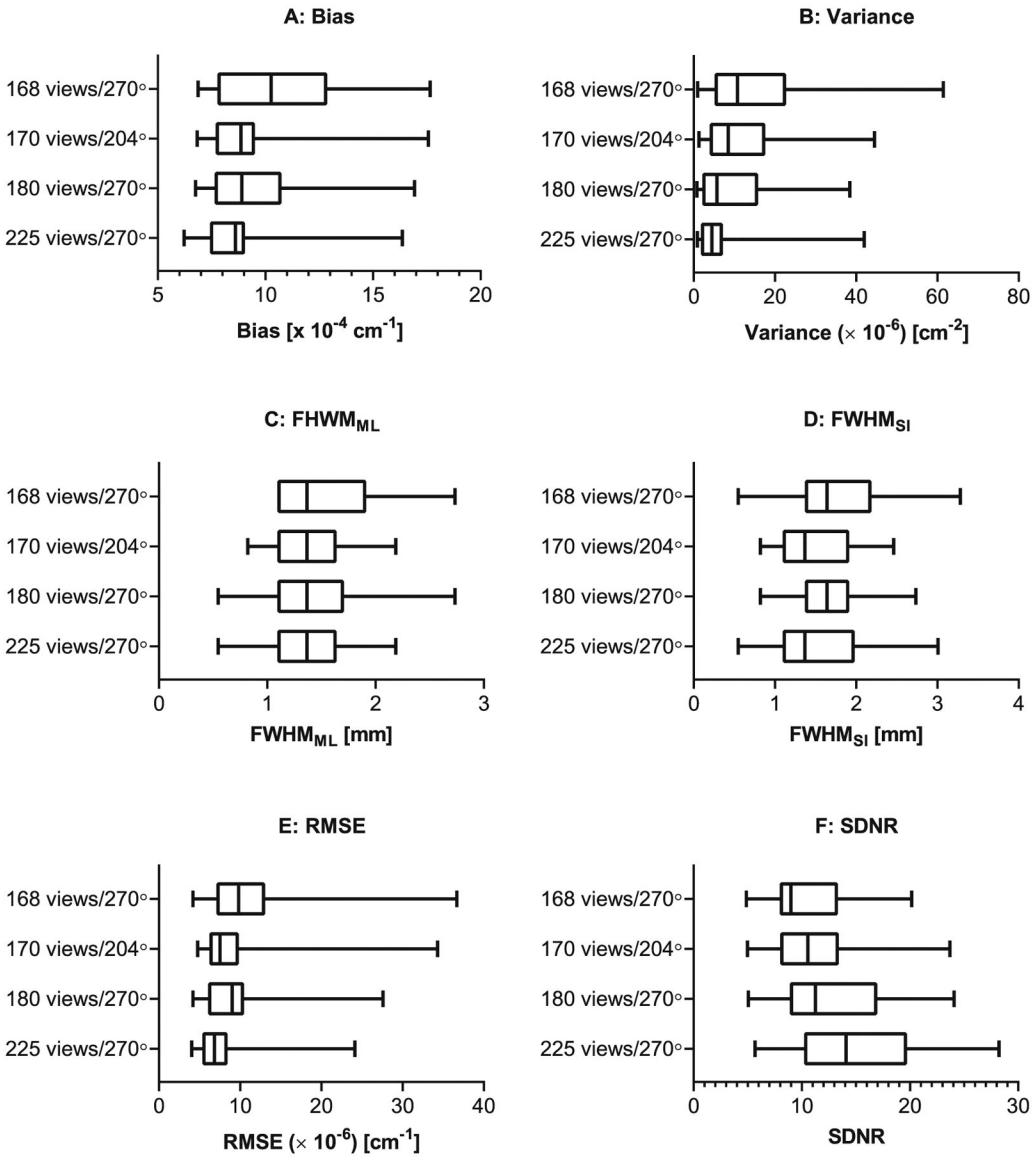

Fig 13.

Box plot of the image quality metrics [A: Bias; B: Variance; C: Full-Width at Half-Maximum (FWHM) of the largest calcification along the mediolateral direction; D: FWHM of the largest calcification along the superior-inferior direction; E: Root Mean Squared Error (RMSE); and F: Signal Difference-to-Noise Ratio (SDNR)]. The box represents the interquartile range, the line within the box denotes the median, and the whiskers correspond to the minimum and maximum.

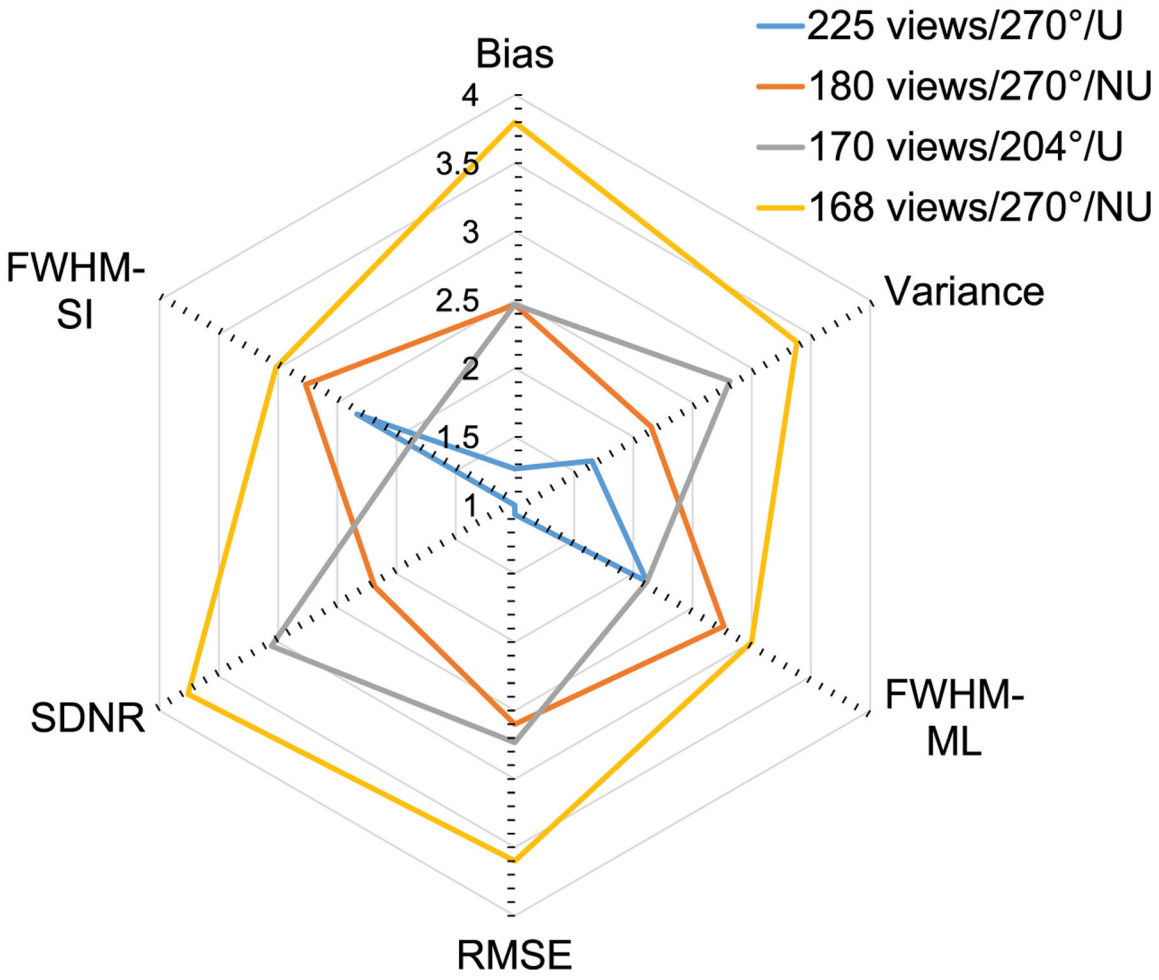

Fig 14.

Radar chart of the short-scan reconstructions. For each image quality metric, the mean rating (n=30 cases) is used to construct the chart for each short-scan reconstruction. A rating of 1 corresponds to the best performance (lowest bias, variance, FWHM and RMSE, and highest SDNR) and a rating of 4 corresponds to the worst among the four short-scan reconstructions. [FWHM: Full-width at Half-Maximum; SDNR: Signal-Difference to Noise Ratio; RMSE: Root Mean Squared Error].

Table 1.

Characteristics of cases included in the study [reported as median (1^{st} quartile – 3^{rd} quartile)].

Age (years)	51 (46 – 57)
Chest-wall to nipple length (cm)	9.9 (7.9 – 11.9)
Diameter at chest-wall (cm)	13.5 (12 – 15.1)
Total breast volume (cm^3)	376.7 (195.3 – 709.6)
Volumetric glandular fraction (%)	10.6 (6.5 – 17.8)
Fibroglandular weight fraction, f_g (%)	11.7 (7.3 – 19.5)
Average glandular dose (mGy)	11.4 (9.9 – 14.4)

Table 2.

Reconstruction time (milliseconds per slice per iteration) for an example case of a large breast with 100 OS-SART iterations and 10 TV iterations.

Sampling scheme	Ray-driven	Voxel-driven	Distance-driven
225 views, 270°	35.8	41.0	69.0
180 views, 270°	30.4	34.4	58.8
168 views, 270°	27.9	31.1	52.3
170 views, 204°	27.0	29.8	50.9

Table 3.

Summary of number of TV iterations used for large, medium, and small breasts.

	225 views, 270°		180 views, 270°		168 views, 270°		170 views, 204°	
	Visual Assessment	**AUP**	**Visual Assessment**	**AUP**	**Visual Assessment**	**AUP**	**Visual Assessment**	**AUP**
Large breast	15	15	15	15	10	10	10	10
Medium breast	10	10	10	10	10	10	15	10
Small breast	5 or 10	10	10	10	5 or 10	10	10	10

Table 4.

Summary statistics of image quality measures from reference full-scan FDK reconstruction (300 views in 360°) and short-scan FIRST reconstructions with 225, 180 and 168 views in 270°, and 170 views in 204°. All metrics are reported as median (1^{st} quartile, 3^{rd} quartile) and were computed using linear attenuation coefficients in units of cm^{-1}. Bias and RMSE were computed with respect to the reference FDK reconstruction. [AGD: Average Glandular Dose; FWHM: Full-Width at Half-Maximum; RMSE: Root-Mean-Squared Error].

	Full-scan (reference)	**Short-scan**				**P-values**
Reconstruction algorithm	**FDK**	**FIRST**				
Angular range	360°	270°			204°	
Number of views	300	225	180	168	170	
Angular sampling	Uniform	Uniform	Non-uniform	Non-uniform	Uniform	
AGD (mGy)	11.4 (9.9, 14.4)	8.5 (7.5, 10.8)	6.8 (6.0, 8.6)	6.4 (5.6, 8.1)	6.4 (5.6, 8.2)	
Variance ($\times 10^{-6}$ cm^{-2})	58.1 (47.4, 87.1)	4.5 (1.7, 7.2)	5.7 (2.1, 15.9)	10.8 (5.2, 22.7)	8.5 (4.0, 17.6)	P<0.0001
SDNR	6.9 (5.4, 7.7)	14.1 (10.2, 19.7)	11.3 (8.9, 17)	9.0 (8, 13.3)	10.6 (8.0, 13.4)	P<0.0001
$FWHM_{ML}$ (mm)	1.37 (1.09, 1.71)	1.37 (1.09, 1.64)	1.37 (1.09, 1.71)	1.37 (1.09, 1.92)	1.37 (1.09, 1.64)	P=0.0003
$FWHM_{SI}$ (mm)	1.37 (1.30, 1.91)	1.37 (1.09, 1.98)	1.64 (1.37, 1.91)	1.64 (1.37, 2.19)	1.37 (1.09, 1.91)	P=0.0006
Bias ($\times 10^{-4}$ cm^{-1})	N/A	8.6 (7.4, 9.0)	8.9 (7.6, 10.7)	10.3 (7.8, 12.9)	8.9 (7.7, 9.5)	P<0.0001
RMSE ($\times 10^{-6}$ cm^{-1})	N/A	6.8 (5.3, 8.4)	9.0 (6.1, 10.5)	9.8 (7.1, 13.1)	7.5 (6.2, 9.8)	P<0.0001